Ocean Dynamics (2017) 67:1195–1216
DOI 10.1007/s10236-017-1083-y

Regionality and seasonality of submesoscale and mesoscale turbulence in the North Pacific Ocean

Hideharu Sasaki[1] · **Patrice Klein**[2] · **Yoshikazu Sasai**[3] · **Bo Qiu**[4]

Received: 29 September 2016 / Accepted: 27 June 2017 / Published online: 13 July 2017

Abstract The kinetic energy (KE) seasonality has been revealed by satellite altimeters in many oceanic regions. Question about the mechanisms that trigger this seasonality is still challenging. We address this question through the comparison of two numerical simulations. The first one, with a 1/10° horizontal grid spacing, 54 vertical levels, represents dynamics of physical scales larger than 50 km. The second one, with a 1/30° grid spacing, 100 vertical levels, takes into account the dynamics of physical scales down to 16 km. Comparison clearly emphasizes in the whole North Pacific Ocean, not only a significant KE increase by a factor up to three, but also the emergence of seasonal variability when the scale range 16–50 km (called submesoscales in this study) is taken into account. But the mechanisms explaining these KE changes display strong regional contrasts. In high KE regions, such the Kuroshio Extension and the western and eastern subtropics, frontal mixed-layer instabilities appear to be the main mechanism for the emergence of submesoscales in winter. Subsequent inverse kinetic energy cascade leads to the KE seasonality of larger scales. In other regions, in particular in subarctic regions, results suggest that the KE seasonality is principally produced by larger-scale instabilities with typical scales of 100 km and not so much by smaller-scale mixed-layer instabilities. Using arguments from geostrophic turbulence, the submesoscale impact in these regions is assumed to strengthen mesoscale eddies that become more coherent and not quickly dissipated, leading to a KE increase.

Keywords Submesoscale turbulence · Scale interactions · Mixed-layer instability · High-resolution simulations · North Pacific

This article is part of the Topical Collection on the *48th International Liège Colloquium on Ocean Dynamics, Liège, Belgium, 23–27 May 2016*

P. Klein is presently a visiting scientist at Caltech/JPL, Pasadena, USA.

Responsible Editor: Ananda Pascual

✉ Hideharu Sasaki
sasaki@jamstec.go.jp

[1] Application Laboratory, JAMSTEC, 3173-25 Showa-machi, Kanazawa-ku, Yokohama, Kanagawa 236-0001, Japan

[2] Laboratoire d'Océanographie Physique et Spatiale, IFREMER-CNRS-UBO-IRD, Plouzane, France

[3] Research and Development Center for Global Change, JAMSTEC, Yokohama, Japan

[4] Department of Oceanography, University of Hawaii at Manoa, Honolulu, HI, USA

1 Introduction

Oceanic eddies (100–300 km) have been monitored by satellite altimeters for more than 25 years. They are now known to explain, not only most of the total ocean kinetic energy (KE) (Ferrari and Wunsch 2009), but also most of the turbulent dispersion and transport of tracers such as heat and carbon dioxide in the global ocean (Lévy et al. 2012a; Haza et al. 2012; Zhong and Bracco 2013). Altimeter data further reveal, in many regions, the existence of significant seasonality of the kinetic energy associated with these mesoscale eddies (eddy kinetic energy or EKE) (Qiu 1999; Zhai et al. 2008; Dufau et al. 2016), often 180° out of phase with the atmospheric forcing (Zhai et al. 2008; Dufau et al. 2016). This has led to question the mechanisms leading to this EKE seasonality.

A first answer has been proposed by several studies (Qiu 1999; Qiu et al. 2008; Capet et al. 2016) invoking the baroclinic instability of large-scale vertical current shears in the upper

oceanic layers with a wavelength of the order of 100 km (see Tulloch et al. 2011). Their explanation is based on the thermocline tilt change caused by the atmospheric forcings. Specifically, Qiu (1999) and Qiu et al. (2008) showed that, in the subtropical gyre of the North Pacific Ocean, the well-stratified upper thermocline in summer/fall is destroyed in winter because of the surface cooling that begins in late October. This leads the upper thermocline tilt to be enhanced and reach a maximum in early spring with an associated increased vertical shear, a favorable situation for a Charney-type baroclinic instability to develop. When the surface buoyancy forcing changes from cooling to heating, a flatter seasonal thermocline builds up, which weakens the vertical shear and, therefore, inhibits baroclinic instability. Qiu (1999) and Qiu et al. (2008) further noted, using altimeter data, that the EKE also experiences a seasonal cycle but with a phase lag of about 2 months behind the seasonal cycle of the thermocline tilt. Analysis of the Argo and altimetry datasets suggests a similar scenario for the density structure south of the Gulf Stream (Capet et al. 2016).

Another explanation invokes the impact of scales smaller than 50 km (called submesoscales in the present study). These scales usually emerge, preferentially in winter, from the instabilities of surface frontal structures (Thompson et al. 2016). Many recent studies suggest mixed-layer instability, with typical unstable wavelengths of 10–40 km (MLI, see Boccaletti et al. 2007; Fox-Kemper et al. 2008; Callies et al. 2016), as the main mechanism explaining the emergence of submesoscales in winter (Capet et al. 2008a; Mensa et al. 2013; Qiu et al. 2014; Sasaki et al. 2014; [hereafter Q14 and S14, respectively]; Callies et al. 2016). They further show that the resulting kinetic energy at submesoscales subsequently cascades to larger scales leading to a maximum EKE around May–June. The resulting EKE spectra are characterized by a winter k^{-2} slope (with k the wavenumber) and a summer k^{-3} slope (Q14; S14). Callies et al. (2015) using ADCP data in the Gulf Stream region reported similar results involving EKE spectra with a k^{-2} slope in winter and a k^{-3} slope in summer, suggesting the presence of more energetic submesoscales in winter.

The present study focuses on the mechanisms that trigger the EKE seasonality in the North Pacific Ocean (NPO). For that purpose, we compare the results of two numerical simulations (described in Section 2), identical except for the resolution. The first one, with a 1/10° horizontal resolution (with 54 vertical levels), does not resolve scales below 50 km and, therefore, does not take into account submesoscales. The second one, with a 1/30° horizontal resolution (with 100 vertical levels), resolves a large part of the submesoscale range (between 16 and 50 km). As shown in Section 3, the two simulations display quite different results, in terms of both magnitude and seasonality, for the relative vorticity, mixed-layer depth (MLD) and EKE fields. Section 4 indicates that, in regions with high EKE—mostly the Kuroshio Extension and subtropics, the seasonality of the ocean dynamics is principally driven by the winter submesoscales. Discussion in Section 5 suggests that, in other regions where EKE is lower, the seasonality of the ocean dynamics is principally driven by larger-scale instabilities. Discussion is offered in the last section.

2 Two numerical simulations of the North Pacific Ocean

The OGCM for the Earth Simulator (OFES) model (Masumoto et al. 2004; Komori et al. 2005) is used to conduct two hindcast simulations at 1/30° (Sasaki and Klein 2012; S14) and at 1/10° (Nonaka et al. 2016) horizontal resolutions [hereafter referred to as the 1/30° simulation and 1/10° simulation, respectively]. This model is based on MOM3 (Pacanowski and Griffies 1999), a hydrostatic ocean model subject to Boussinesq and hydrostatic approximations. The number of vertical levels is 100 (54) for the 1/30° (1/10°) simulation. A biharmonic operator dumps numerical noises and vertical mixing makes use of a scheme developed by Noh and Kim (1999). Biharmonic viscosity and diffusion coefficients are, respectively, 1.0×10^9 m^4 s^{-1} (2.7×10^{10} m^4 s^{-1}) and 3.3×10^8 m^4 s^{-1} (9.0×10^9 m^4 s^{-1}) in the 1/30° (1/10°) simulation. The model domain covers the North Pacific Ocean with a meridional coverage from 20° S to 68° N and a zonal coverage from 100° E to 70° W. The climatological integration of the 1/10° simulation for 15 years was first conducted by using long-term mean 6-hourly atmospheric data from 1979 to 2004 of Japanese 25-year reanalysis (Onogi et al. 2007). The hindcast simulation from 1979 to 2012 followed this climatological simulation. The 1/30° simulation started from the regrided output of the 1/10° simulation on January 1, 2000, and ended on December 31, 2003. The spin-up period for the upper ocean circulation for the 1/30° simulation is less than 1 year. Consequently, only outputs from the period from January 1, 2001, to December 31, 2003, are analyzed in this study.

A numerical simulation with a given horizontal resolution allows to capture correctly the physics of wavelengths of at least 5 times this resolution (Lévy et al. 2012b). This means that the 1/10° and 1/30° simulations capture the physics of wavelengths, respectively, larger than 50 and 16 km. KE associated with submesoscales (<50 km) is known to result from mechanisms such as frontogenesis, wind-driven frontal instabilities, mixed-layer instabilities (MLIs), and others (see Haines and Marshall 1998; McWilliams 2016; Thompson et al. 2016). Observational studies further emphasize that these instabilities are mostly efficient in winter and negligible in summer (Thompson et al. 2016; Buckingham et al. 2016). At last, many studies (Q14; S14; Callies et al. 2016; Thompson et al. 2016) suggest that winter submesoscales are mostly generated by MLI because of the larger MLD during this period (Boccaletti et al. 2007; Fox-Kemper et al.

2008). To better understand whether our two simulations resolve or not MLIs, we have estimated the most unstable MLI wavelengths (Stone 1966; Nakamura 1988) in the whole NPO as a function of time using the same method as in Fox-Kemper et al. (2008) (see also S14). Figure 1a–c indicates winter values (December through February) larger than 20–25 km. These wavelengths are well resolved in the 1/30° simulation but not in the 1/10° simulation. Consequently, comparison between the two simulations allows to diagnose the impacts of the winter "MLI" submesoscales on the NPO ocean dynamics. All the dynamical fields analyzed in the next sections have been averaged over a 1-day period in order to filter out near-inertial motions.

3 Basin-scale impacts of submesoscales

Surface frontal structures are usually associated with intensified along-front jets and, therefore, are often exhibited in the relative vorticity (RV) field. In such frontal dynamics, RV characterizes the size of these structures and their dynamics since smaller-scale surface frontal structures exhibit larger RV (Held et al. 1995) (and, therefore, larger Rossby number, *Ro*, with *Ro* defined as $Ro = \zeta/f$, ζ being the relative vorticity and f the Coriolis frequency), leading to large vertical velocities (Klein and Lapeyre 2009).

Figure 2a, b reveals the emergence of a strong and conspicuous seasonality in the RV field of the 1/30° simulation. This seasonality is characterized by much smaller scales with larger amplitudes in winter (with *Ro* reaching values of order one) compared to summer, suggesting the presence of energetic submesoscales in winter. However, this seasonality has not the same intensity everywhere. The northern part of the NPO and some areas in the eastern part have much weaker *Ro* magnitude but still exhibit a nonnegligible seasonality as discussed later. On the other hand, no seasonality is observed in the 1/10° simulation in which the RV field displays much weaker amplitudes and larger scales (Fig. 2c, d).

It is well recognized, since Hakim et al. (2002), that the submesoscale turbulence triggered by surface frontal instabilities (including MLI) leads to positive (up-gradient) buoyancy fluxes and, therefore, to a restratification of the upper oceanic layers (Lapeyre et al. 2006; Boccaletti et al. 2007; Fox-Kemper et al. 2008; McWilliams et al. 2009; S14; Callies et al. 2016). To further characterize this impact, we have compared the winter MLD[1] fields in both simulations. Areas with large MLD (>200 m) (Fig. 3a, b) are patchy to the south and north of the Kuroshio Extension region (KET), which is consistent with the hydrographic and Argo float observations (Suga et al. 2004; de Boyer Montégut et al. 2004). In the eastern subtropical region (around 140° W and 25° N) where the subtropical mode water is ventilated (e.g. Hautala and Roemmich 1998; Hanawa and Talley 2001), MLD is deep compared with the surroundings, which is also consistent with observations. The submesoscale impact on the restratification is revealed by Fig. 3c that shows the winter MLD differences between the two simulations. In KET, the subtropical regions, and also the mid-latitude region in the eastern part, MLD is shallower in the 1/30° simulation than in the 1/10° simulation (with a difference that can exceed 100 m). This highlights a strong restratification impact in regions where large RV magnitude with a strong seasonality is observed (Fig. 2a, b). However, in the northern parts of the NPO (west and east), in particular in the northern part of the Kuroshio Extension, MLD is conspicuously larger in the 1/30° simulation, indicating submesoscales contribute to deepen the mixed layer instead of shallowing it.

The positive buoyancy fluxes, associated with submesoscales, also correspond to a net transformation of potential energy (PE) into KE. Some studies (Fox-Kemper et al. 2008; Q14; S14; Callies et al. 2016) further suggest that this KE flux at submesoscales is transferred to larger scales (through the inverse KE cascade) and, therefore, feeds up KE of mesoscale eddies. Therefore, it is pertinent to question the EKE differences between our two simulations. Figure 4a, b displays the EKE, averaged over the 2001–2003 period, in both simulations, with Fig. 4c showing the EKE difference. In agreement with satellite altimeter observations (Zhai et al. 2008), Fig. 4a, b displays a high EKE level along the KET region, a moderate level in subtropical regions including along the Subtropical Countercurrent (STCC) (EKE is reduced by a factor 2 to 4 compared with the KET region), and a lower level (reduced by a factor 10) in other areas including the subarctic and eastern mid-latitude regions. But Fig. 4c reveals that taking into account submesoscales leads to an EKE increase by a factor close to 2 in the KET and western and eastern subtropical regions. Other regions with smaller EKE experience as well an EKE increase (with also a factor 2) in the 1/30° simulation, but this increase is not so well displayed in Fig. 4c because of the color scale. The factor 2 increase is consistent with the results from similar numerical experiments in the North Atlantic Ocean designed to assess the impact of small scales (E. Chassignet, personal communication). Furthermore, in all regions of the NPO, EKE time evolution (Fig. 5) reveals a significant seasonality in the 1/30° simulation, with a spring-summer maximum, consistent with satellite observations (Zhai et al. 2008; Dufau et al. 2016). No EKE seasonality is observed in the 1/10° simulation.

These EKE results point to the pertinence of the question raised in the introduction: which mechanisms associated with submesoscales (16–50 km) trigger the EKE seasonality and EKE magnitude increase. Figures 1, 2, 3, and 4 emphasize the existence of two classes of regions in the NPO: regions with large EKE and energetic submesoscales (large RV values)

[1] The MLD is defined as the depth at which potential density is different from the sea surface density by 0.03 σ_θ.

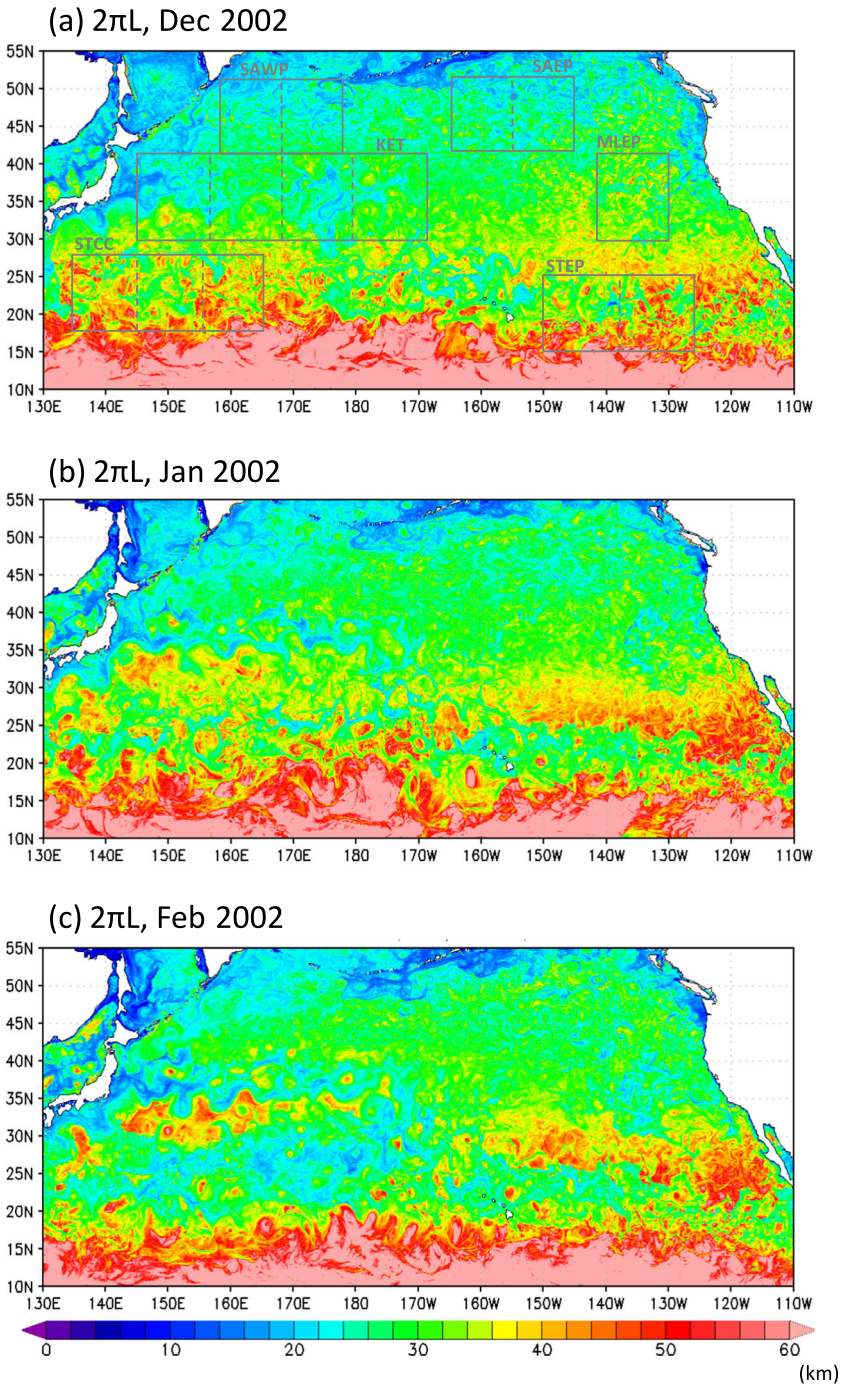

Fig. 1 Unstable MLI wavelength (km) ($2\pi L$, $L^2 = N^2 h^2(1 + Ri)/f^2$, where N, h, Ri, and f are the buoyancy frequency, MLD, Richardson number, and Coriolis frequency, respectively). **a** December, **b** January, and **c** February in 2002

leading to a mixed-layer shallowing, and others, with weaker EKE and less energetic submesoscales leading to a weaker ML shallowing or to a mixed-layer deepening. We next address this question in each of these two classes. Our analyses are conducted in six specific regions sketched in Fig. 1a: three of them corresponding to the first class namely the KET, STCC, and Subtropical Eastern Pacific (STEP) regions, and the other three corresponding to the second class namely the Mid-latitude Eastern Pacific (MLEP), Subarctic Western Pacific (SAWP), and Subarctic Eastern Pacific (SAEP) regions.

Fig. 2 Surface relative vorticity (1e-5 s^{-1}) estimated from velocities on **a**, **c** ▶ March 1 and **b**, **d** September 1, 2002, in the **a**, **b** 1/30° and **c**, **d** 1/10° simulations. Analyses in this study are conducted in the boxes with subboxes, respectively: Kuroshio Extension (KET, 144° E–168° W and 30–42° N), Subtropical Countercurrent (STCC, 135–165° E and 18–28° N), Subtropical Eastern Pacific (STEP, 150–126° W and 15–27° N), Mid-latitude Eastern Pacific (MLEP, 142–130° W and 30–42° N), Subarctic Western Pacific (SAWP, 158–178° E and 42–52° N), and Subarctic Eastern Pacific (SAEP, 165–145° W, 42–52° N) boxes shown in **a**

(a) 1/30° simulation on Mar 1, 2002

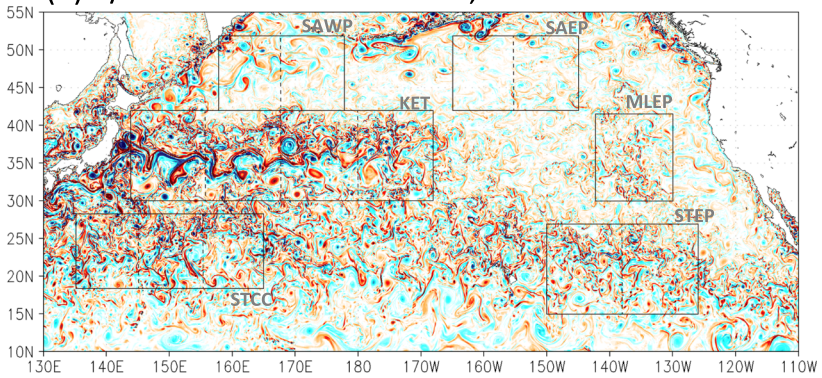

(b) 1/30° simulation on Sep 1, 2002

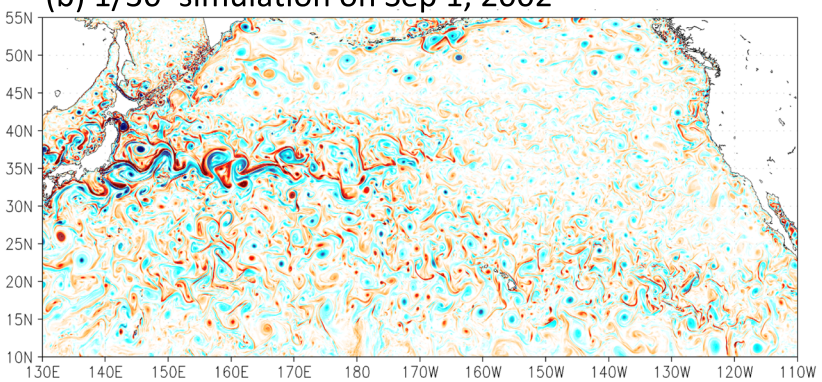

(c) 1/10° simulation on Mar 1, 2002

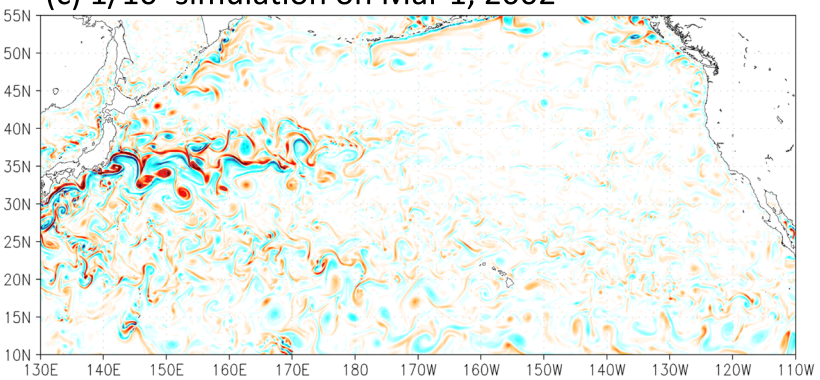

(d) 1/10° simulation on Sep 1, 2002

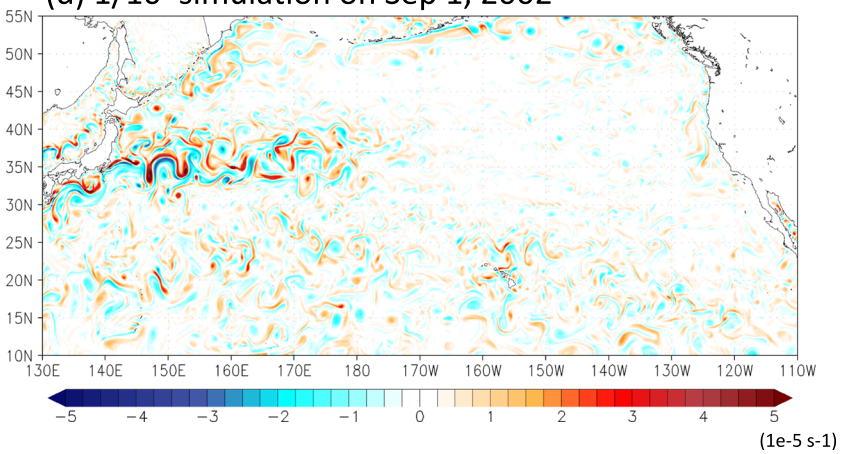

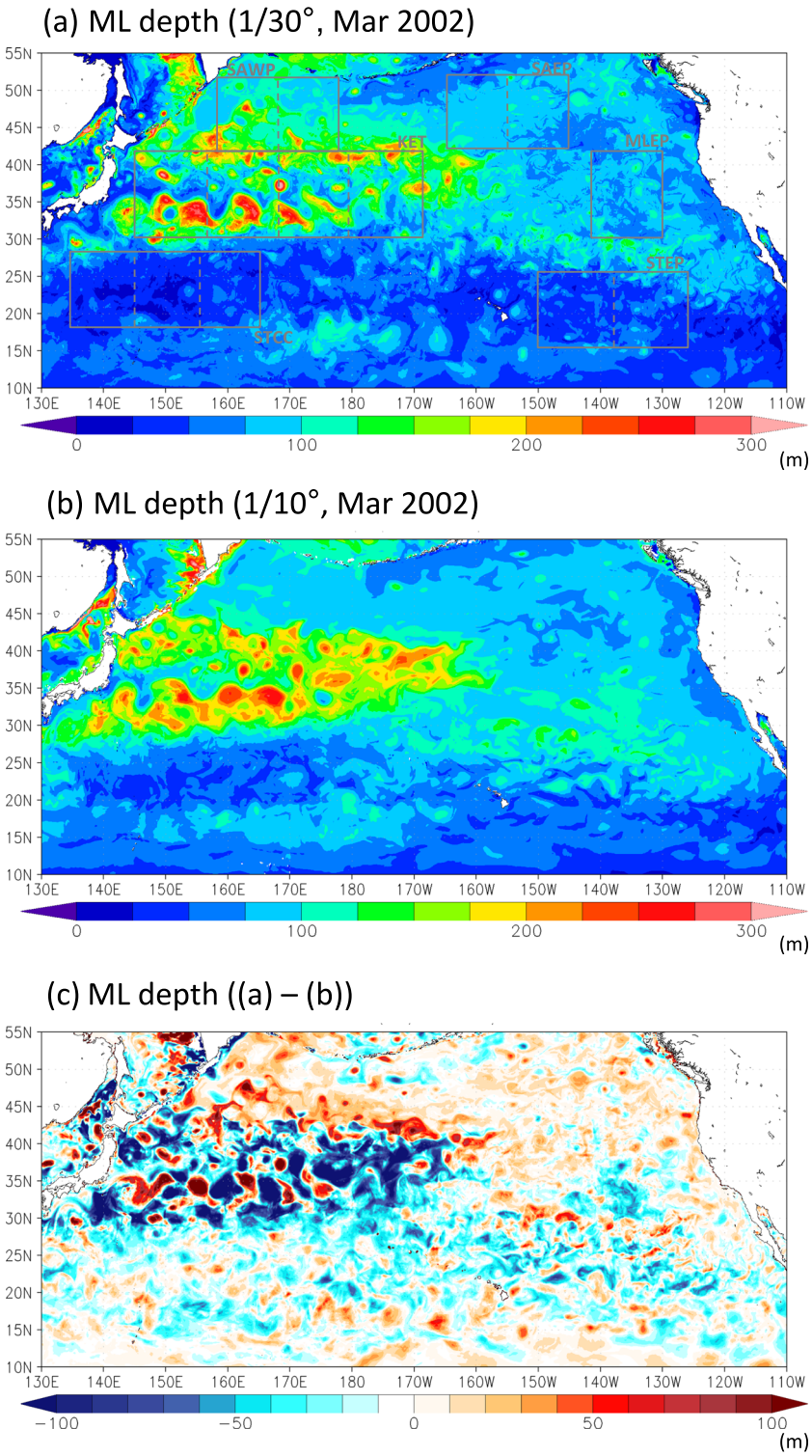

Fig. 3 MLD (m) in March 2002 in the **a** 1/30° and **b** 1/10° simulations. The MLD is defined as the depth at which potential density is large by 0.03 σ_θ from the density at surface. **c** Difference of the MLD (a – b)

4 Impacts of submesoscales in high EKE regions

The first three regions (KET, STCC, and STEP) experience a significant RV seasonality in the 1/30° simulation with *Ro* rms values up to 0.2 and seasonal amplitude varying with a factor 1.5 to 2 between winter and summer (Fig. 6a–c). The vertical velocity (*W*) time series exhibit a similar seasonality with a factor 3 amplitude. On the other hand, without submesoscales (1/10° simulation), these two quantities conspicuously display almost no or a very weak seasonality. Not surprisingly, the MLD exhibits a strong seasonality in both simulations, but its winter magnitude is smaller in the 1/30° simulation as

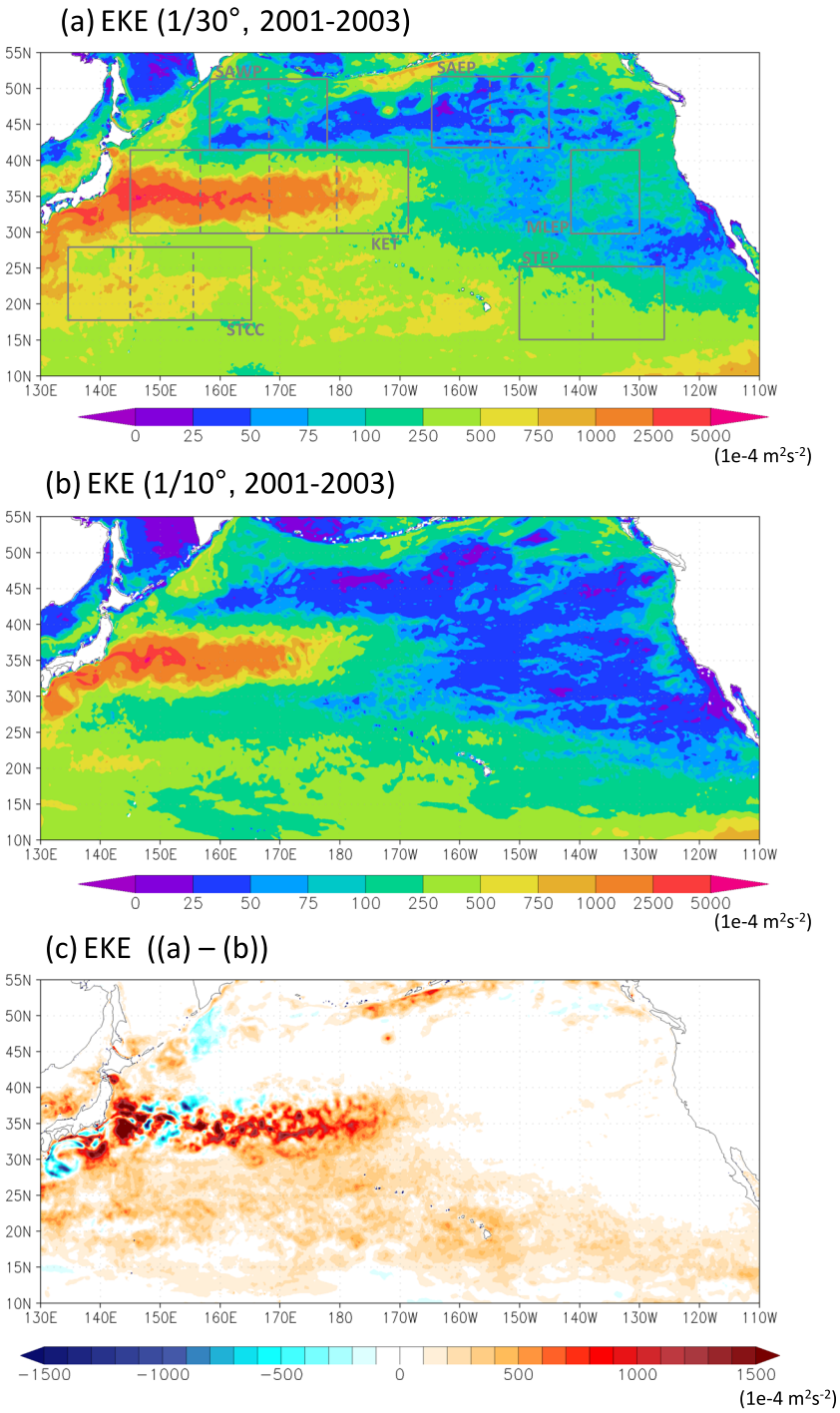

Fig. 4 EKE (1e-4 m^2 s^{-2}) estimated from surface velocity anomalies from 2001 to 2003 in the **a** 1/30° and **b** 1/10° simulations. **c** Difference of the EKEs (a − b)

already noted in Fig. 3. As in S14, there is a lag of about 1 month between RV and MLD (and *W*) time series: MLD and *W* time series exhibit a similar seasonality and a sudden decay in late winter not observed for RV. One explanation (see S14 for details) is that the RV field, after the abrupt decay of MLD and *W*, evolves as a two-dimensional turbulent flow in free decay. Figure 7 shows meridional sections of *W* in winter, respectively, in the western and eastern parts of the North Pacific Ocean. They illustrate the larger magnitude but also the smaller scales of this field in the 1/30° simulation compared to the 1/10° simulation. They also emphasize that *W* involves smaller scales in upper layers than in deeper layers. These results suggest that MLD drives the RV evolution (Fig. 6a–c) and, therefore, the production of small scales.

Characteristics of these time series in winter, in particular their phase relationship, strongly suggest MLI as the main mechanism explaining the emergence of submesoscales in the 1/30° simulation. Indeed, the most unstable MLI

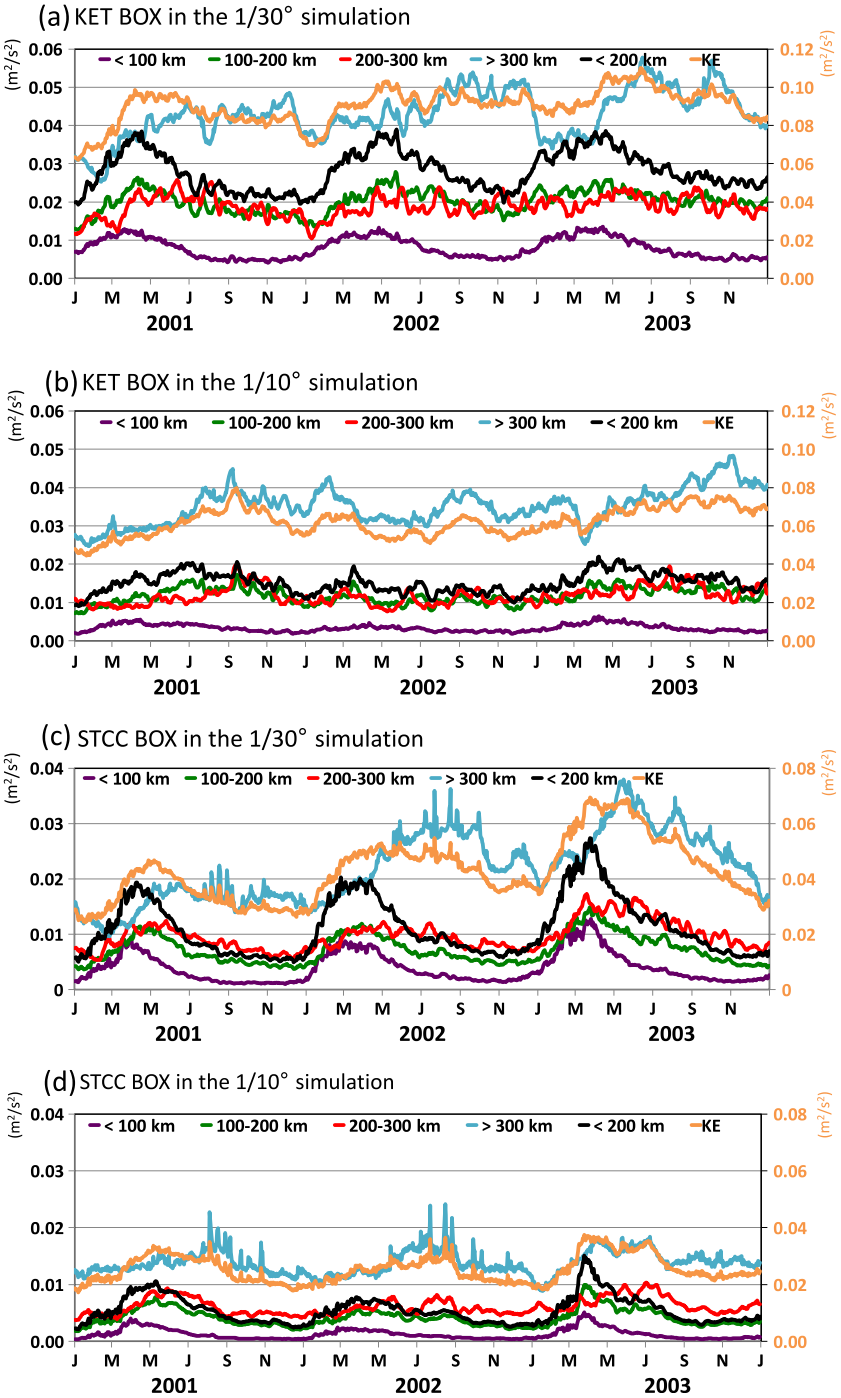

Fig. 5 Time series of EKE ($m^2\ s^{-2}$) from 2001 to 2003 in the **a**, **b** KET; **c**, **d** STCC; **e**, **f** STEP; **g**, **h** MLEP; **i**, **j** SAWP; and **k**, **l** SAEP boxes. EKE in the scale ranges of (*purple*) <100 km, (*green*) 100–200 km, (*red*) 200–300 km, (*blue*) >300 km, and (*orange*) all lengths. The *right* (*left*) *vertical axis* is the scale for the KE of all length (other scales). **a**, **c**, **e**, **g**, **i**, **k** The 1/30° simulation. **b**, **d**, **f**, **h**, **j**, **l** 1/10° simulation. Note that the *vertical scales* in each figure are different

wavelength in the first three regions (KET, STCC, and STEP) is larger than 20–30 km in winter (Fig. 1) except in a small area close to Japan where it is smaller. To confirm this in all three regions, we plotted the time series of the buoyancy fluxes ($<w'b'>_{xy}$ with w', b', and $<*>_{xy}$, respectively, the vertical velocity, buoyancy anomaly, and horizontal average operator over each region) as a function of depth (Fig. 8). The buoyancy fluxes represent the transformation of PE into KE. The flux is mostly positive and strongly intensified within the mixed layer with a larger magnitude in winter than in summer. This emphasizes the significant KE source within the mixed layer that is present in the 1/30° simulation.

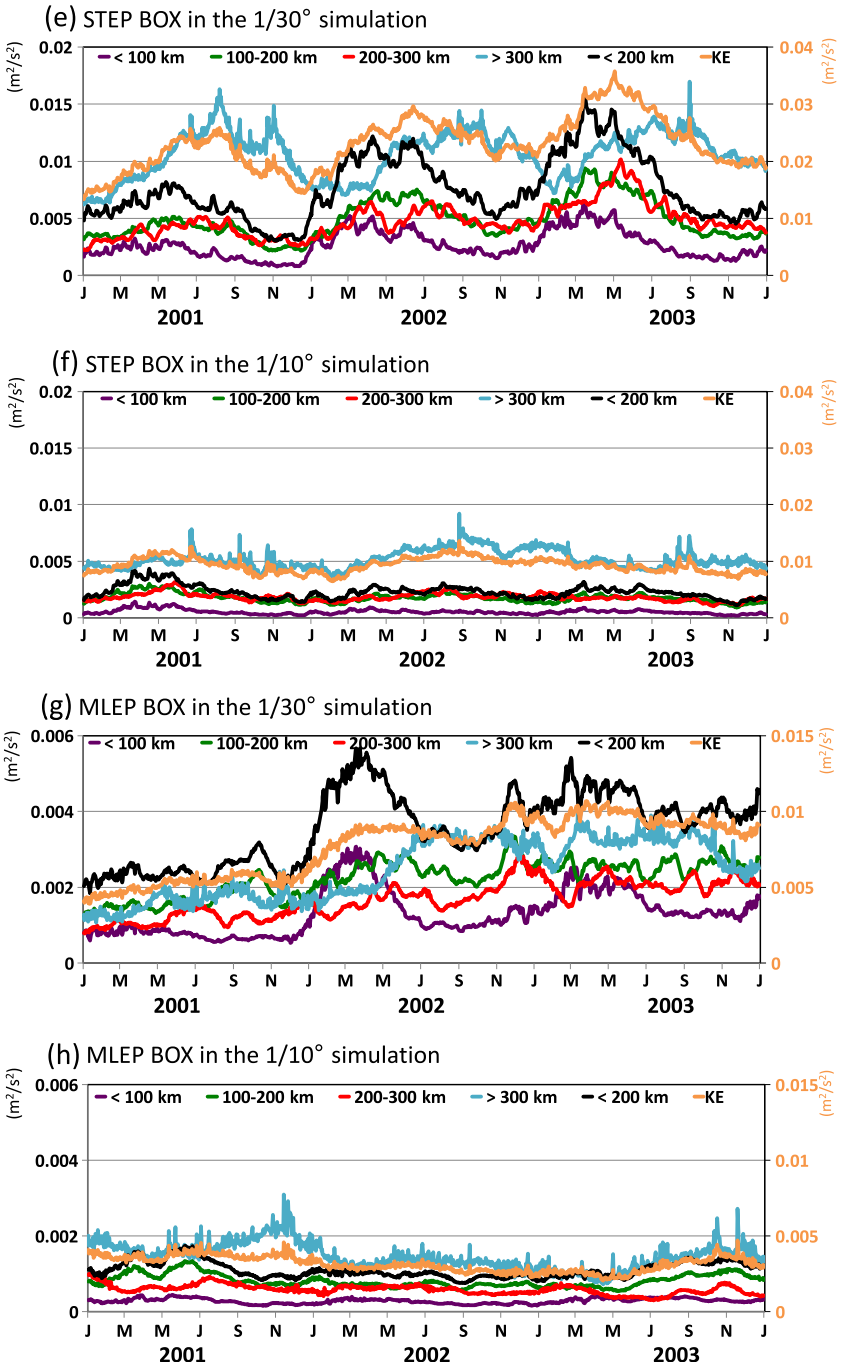

Fig. 5 (continued)

Figure 9 shows the spectra of the buoyancy fluxes within the mixed layer:

$$\mathrm{PK} = \frac{1}{\mathrm{MLD}} \int_0^{-\mathrm{MID}} \left\langle w' b' \right\rangle_{xy} \mathrm{d}z \qquad (1)$$

in the 1/30° simulation. Note that the PK spectrum is different from the co-spectrum of w' and b' integrated over the ML used for a spectral energy budget analysis (e.g., Capet et al. 2008c). Since this paper does not focus on the spectral energy budget, we chose the PK spectrum that is much easier to compute. In the KET, STCC, and STEP regions, the winter spectra peaks are close to 25–40 km. These wavelengths at submesoscale match the estimation displayed in Fig. 1. These results suggest that the winter buoyancy flux, mostly positive within the mixed layer (Fig. 8), has the spectral peak at submesoscale in the high EKE regions.

Figure 10 displays the spectra of winter and summer W within the ML. The 1/30° simulation highlights small

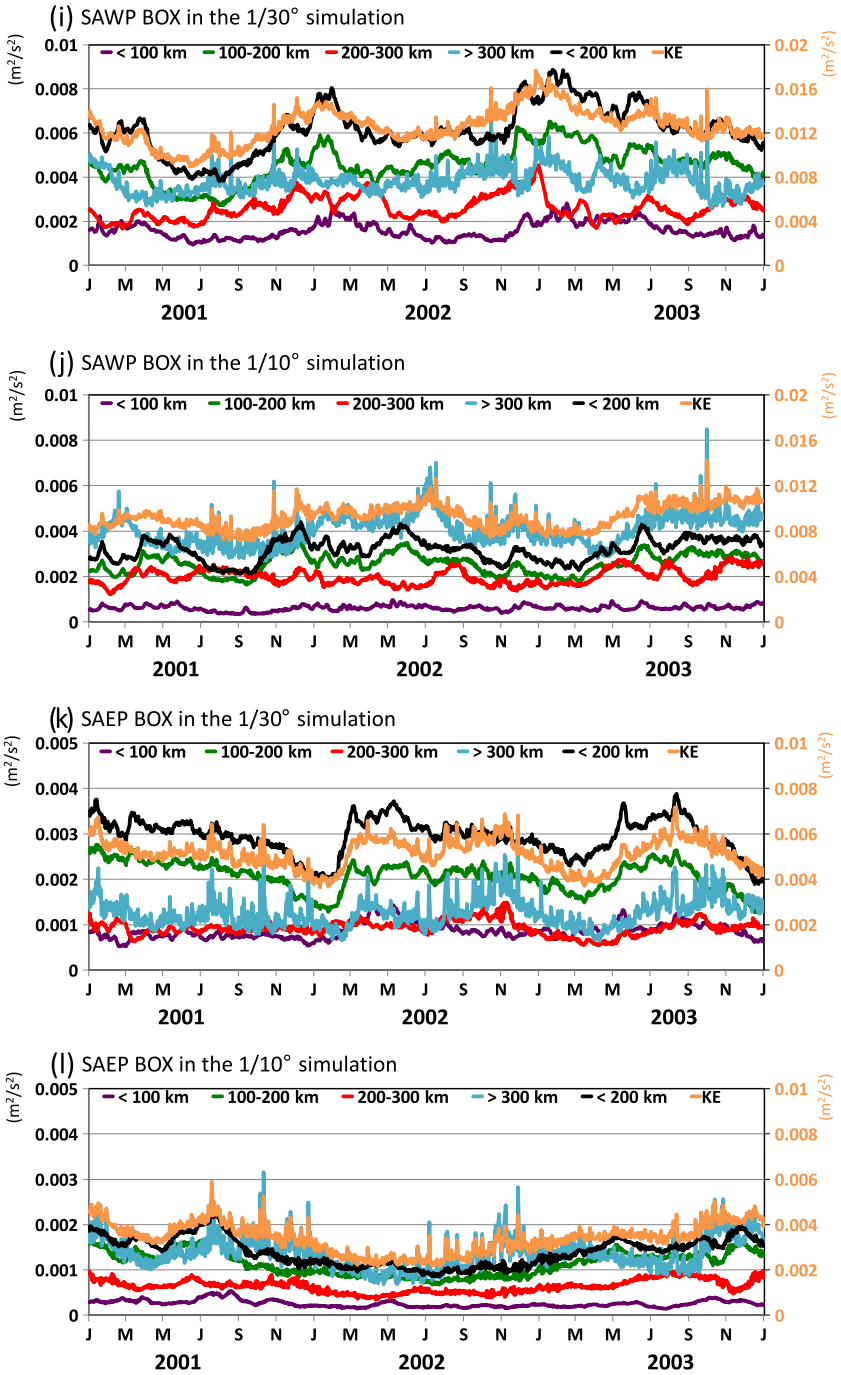

Fig. 5 (continued)

energetic wavelengths at submesoscale in winter. In the KET, STCC, and STEP regions, winter spectral peaks (Fig. 10a–e) are close to 25–40 km, which are similar to those in the PK spectra (Fig. 9a–c). These results suggest that the large vertical motions at small scales are generate by the buoyancy fluxes within the mixed layer in winter. This confirms that winter MLI is the main mechanism that triggers submesoscales leading to a seasonal RV variation and to a restratification of the mixed layer. However, in the 1/10° simulation, winter and summer W spectral peaks have scales close to or larger than 100 km in the KET and STEP regions. In the STCC region, the spectral peak emerges at 50 km in winter and 200 km in summer. This is consistent with the length scale of the Charney instability invoked in Qiu (1999) and Qiu et al. (2008).

At depths below the mixed layer, a spectral analysis of W in the 1/30° simulation (not shown) indicates steeper slopes and peaks at larger scales (>100 km) both in winter and summer

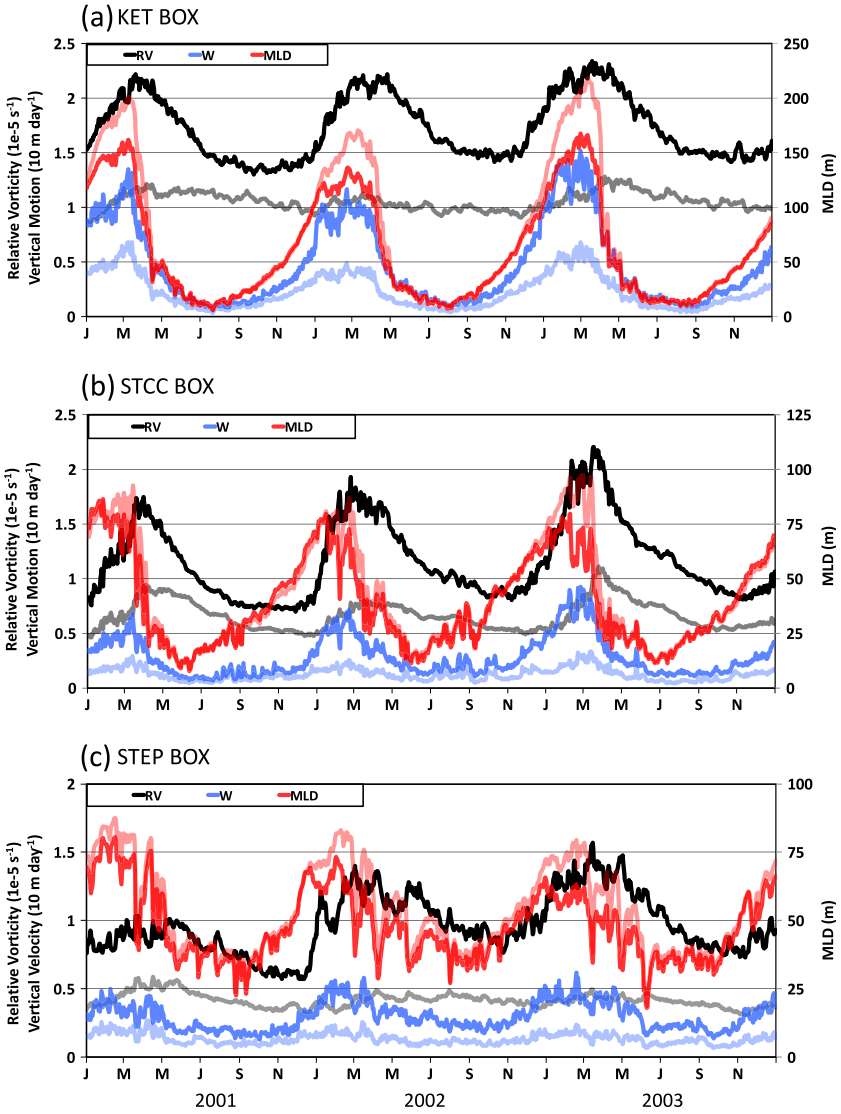

Fig. 6 Time series of (*black curve*) relative vorticity rms (1e-5 s^{-1}), (*blue curve*) vertical velocity rms (10 m day^{-1}), and (*red curve*) MLD (m) from 2001 to 2003 in the boxes of **a** KET, **b** STCC, **c** STEP, **d** MLEP, **e** SAWP, and **f** SAEP. (*Solid color curves*) 1/30° simulation and (*pastel color curves*) 1/10° simulation

with the magnitude larger in winter than in summer. These results are consistent with the vertical sections of the buoyancy flux $\langle w'b' \rangle_{xy}$ as a function of time (Fig. 8). The buoyancy flux is mostly positive and strongly intensified within the mixed layer with a larger magnitude in winter than in summer. This further emphasizes the significant KE source within the mixed layer driving submesoscale motions that is present in the 1/30° simulation.

Spectral KE fluxes (see Capet et al. 2008c; Klein et al. 2008; Sasaki and Klein 2012 for their equations (2) and (3)) (Fig. 11) and EKE time series (Fig. 5) allow to characterize how the KE generated at submesoscale is transferred to other scales through the nonlinear interactions (S14, Q14). The spectral KE fluxes in Fig. 11a–c reveal a net KE transfer to larger scales starting at 25 km. This transfer is characterized by a strong seasonality, in terms of amplitude and width, with a winter intensification due to the impact of submesoscales. In the three regions, magnitude of the net upscale KE transfer increases from 25 up to 150–200 km and then decreases. The corresponding KE fluxes vary by a factor 2 to 3 between the KET region and the two other regions. In order to characterize the time scale of this KE transfer, we next analyze the impact of this transfer on the KE using the same methodology as in S14: KE is partitioned into four wavebands: the 10–100, 100–200, 200–300, and 300–1000 km wavebands. Comparison of the KE time series in the 1/30° and 1/10° simulations (Fig. 5) reveals that presence of submesoscales leads, in all regions, to a significant EKE increase for all scales smaller than 300 km. The increase factor is 1.8, 1.8, and 2.7, respectively, for the KET, STCC, and STEP regions, which agrees with Fig. 4c.

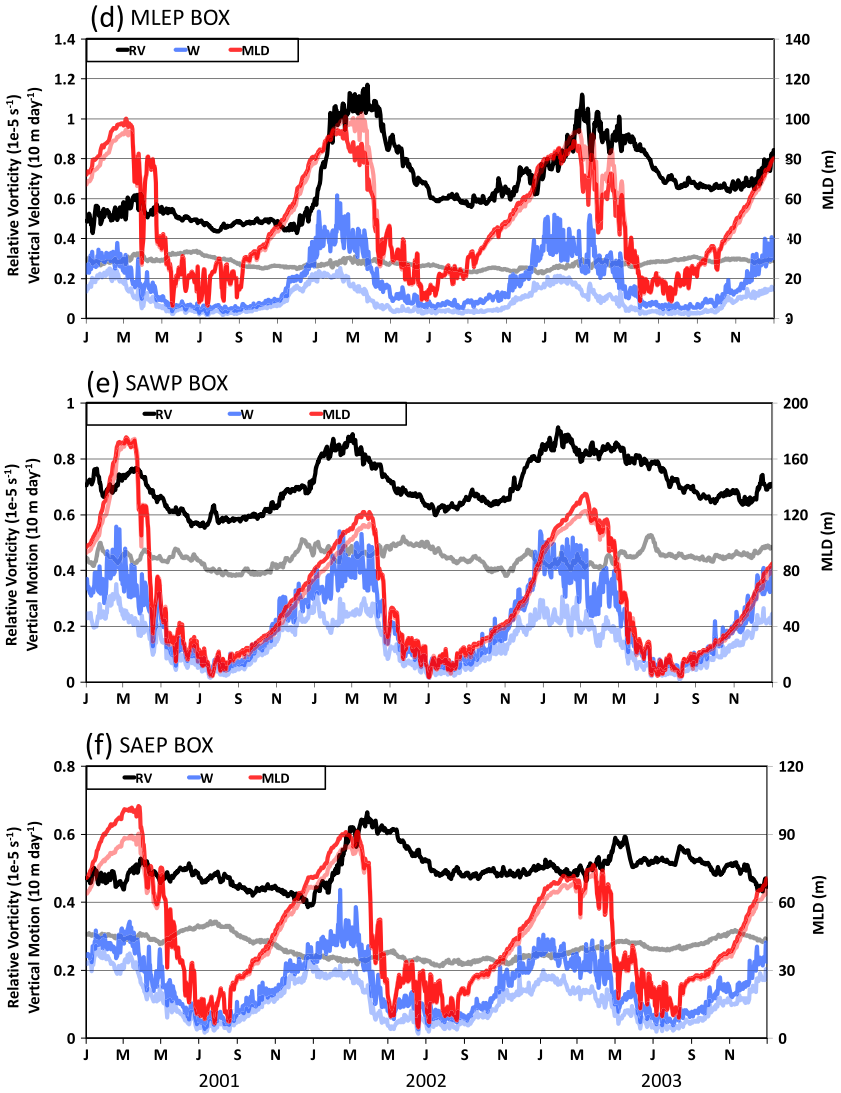

Fig. 6 (continued)

These three regions exhibit in the 1/30° simulation a strong EKE seasonality (with seasonal amplitudes relative to the mean value close to one) for scales up to 300 km. Without submesoscale impact (1/10° simulation), both the mean value and seasonal amplitude of EKE are much smaller (Fig. 5). One interesting characteristic is that the EKE maximum for each waveband occurs with a lag of about 1 month compared with the time series for smaller scales (maximum is approximately attained in March, April, and May, respectively, for the 0–100, 100–200, and 200–300 km wavebands). These lags actually correspond to the time it takes for the KE to be transferred for one waveband to the next one through the inverse KE cascade (as displayed for the three regions in Fig. 11a–c, see also Vallis 2006). All these diagnoses suggest that winter MLI is the main mechanism leading to a significant KE seasonality for scales smaller than 300 km.

Scales larger than 300 km contain not only large eddies but also large-scale evolving currents such as meanders. Comparison between the two simulations reveals an EKE increase in the 1/30° simulation in this waveband smaller than in others (Fig. 5). The largest increase is in the subtropics: STCC (factor 2) and STEP (factor 1.6) (Fig. 5c–f). This increase factor is only 1.2 in the KET region (Fig. 5a, b). As a result, although EKE in this waveband well dominates other wavebands in the 1/10° simulation, its contribution to the total EKE in the 1/30° simulation is much reduced. In terms of time variability, a significant EKE seasonality for these large scales is observed only in the two subtropical regions in both simulations with the peak amplitude being in August–September (Fig. 5c–f). Thus, the larger production of submesoscale KE in the 1/30° simulation appears to impact largest scales in both subtropical regions through the spectral KE fluxes. This result is consistent with Chen et al. (2014) indicating that eddy-mean flow interactions are "local" in subtropical gyres. In the KET region (Fig. 5a, b), although a more significant time variability of the EKE for scales larger than 300 km is observed in the

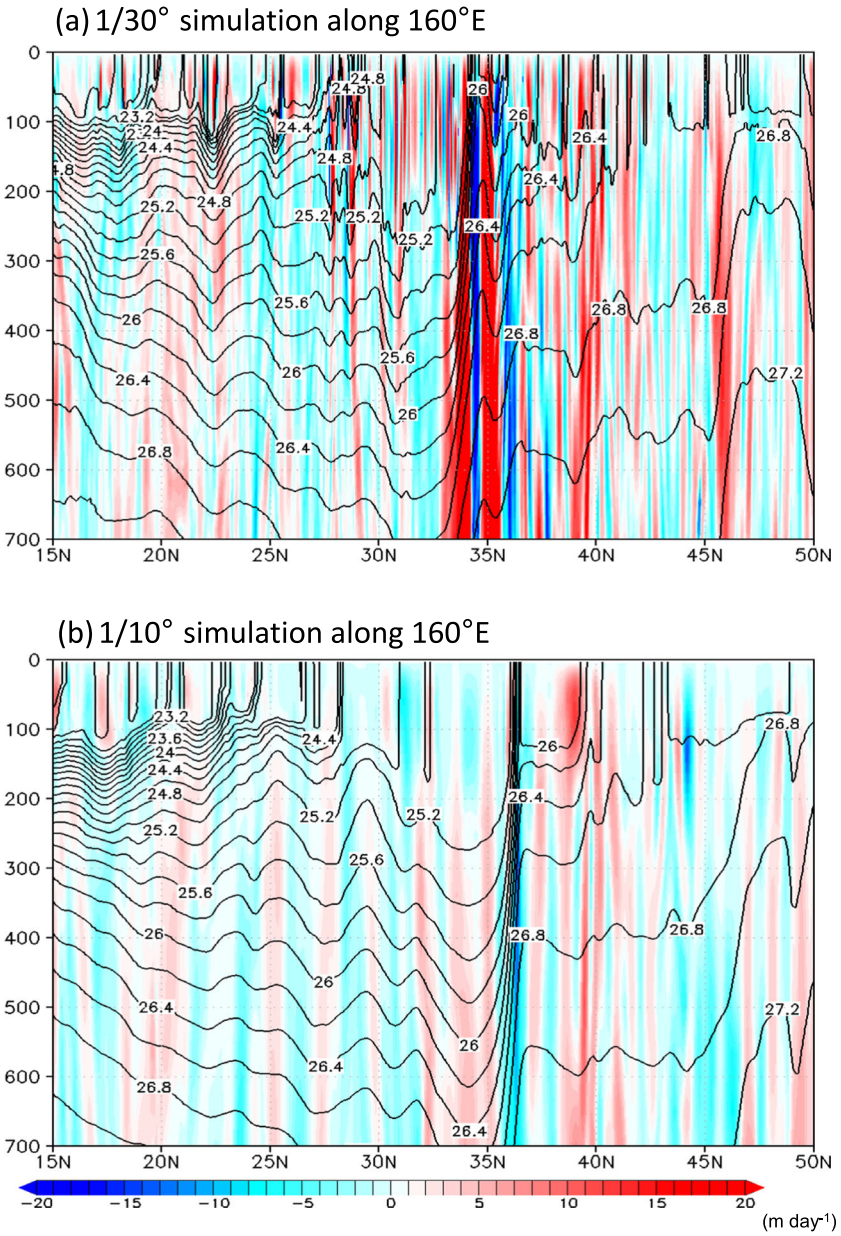

Fig. 7 Meridional sections (from 15° N to 50° N) of the vertical velocity (m day^{-1}, in color) and the potential density (σ_θ, isolines) on March 1, 2002, at **a**, **b** 160° E and **c**, **d** 135° W in **a**, **c** the 1/30° simulation and **b**, **d** the 1/10° simulation

1/30° simulation, no clear seasonality emerges contrary to other wavebands. Other mechanisms, such as EKE fluxes to or from other regions, may explain the EKE characteristics in this waveband. These mechanisms are invoked by Chen et al. (2014) for the KET, which they refer to as "nonlocal" processes.

5 Impacts of submesoscales in regions with lower EKE

In the three other regions (MLEP, SAEP, and SAWP), the most unstable MLI wavelengths are still larger than 20–30 km in winter (Fig. 1). However, the diagnostic analyses in this section indicate that the MLI impact on the ocean dynamics in winter is much weaker than in high EKE regions.

The MLEP region is, however, the one that most resembles the high EKE regions. It experiences a RV seasonality in the 1/30° simulation with a seasonal amplitude varying with a factor between 1.5 and 2 between winter and summer and with, however, smaller magnitudes (Fig. 6d) than in the first three regions with higher EKE (Fig. 6a–c). The vertical velocity (W) time series exhibits a similar seasonality with a factor 2–3 amplitude and is in phase with the MLD time series. The meridional section of W in winter in the eastern North Pacific Ocean also illustrates the larger magnitude but also the smaller

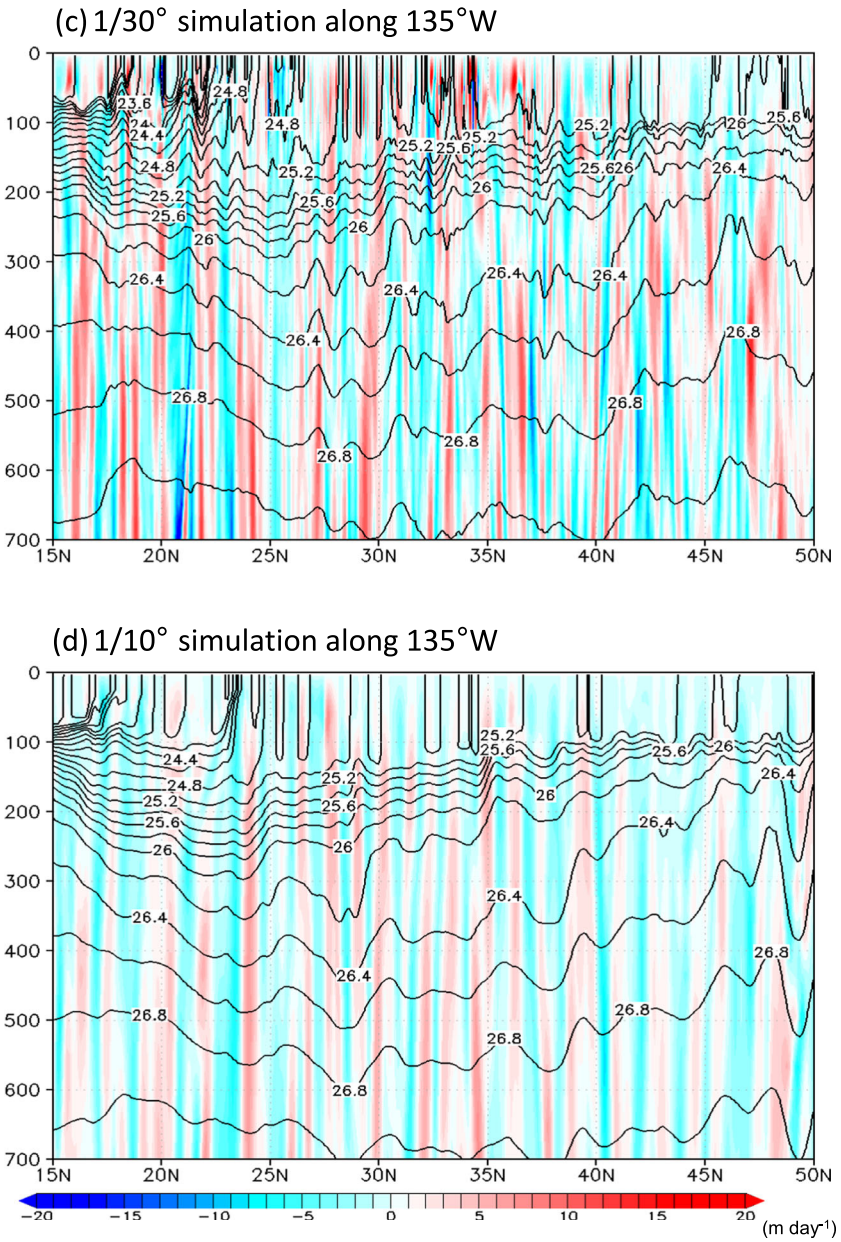

Fig. 7 (continued)

scales in the MLEP region (30–42° N) in the 1/30° simulation (Fig. 7c) compared to the 1/10° simulation (Fig. 7d). Again, there is a phase lag of about 1 month between RV and MLD times series (Fig. 6d), suggesting that MLD drives MLIs and, therefore, the production of submesoscales. Not surprisingly, without submesoscales (1/10° simulation), RV and *W* time series display a much weaker seasonality. The differences between the winter MLD in the two simulations emphasize the submesoscale impact on the restratification of the mixed layer. But this restratification is much weaker than in the high EKE regions (Fig. 6a–c) (less than 10%).

Characteristics of these time series in winter, in particular their phase relationship (see S14), suggest that winter MLIs are still active. To confirm the MLI impact, we again analyze the buoyancy flux (PK) spectra, which represents transformation of PE into KE within the mixed layer. From Fig. 9d, there are now two winter spectral peaks in the 1/30° simulation, at 100 and at 20 km (instead of one around 25–40 km in high EKE regions; Fig. 9a–c). The resultant vertical motion *W* also displays the two peaks at the same scales (Fig. 10g). However, the 1/10° simulation displays just one winter spectral PK peak at 100 km (Fig. 10h). Figure 8d confirms the strong seasonality of the transformation of PE into KE with a positive sign. Spectral KE fluxes in Fig. 11d reveal a net KE transfer to larger scales starting at 20 km. But magnitudes of these fluxes in this lower KE region are, not surprisingly, more than three

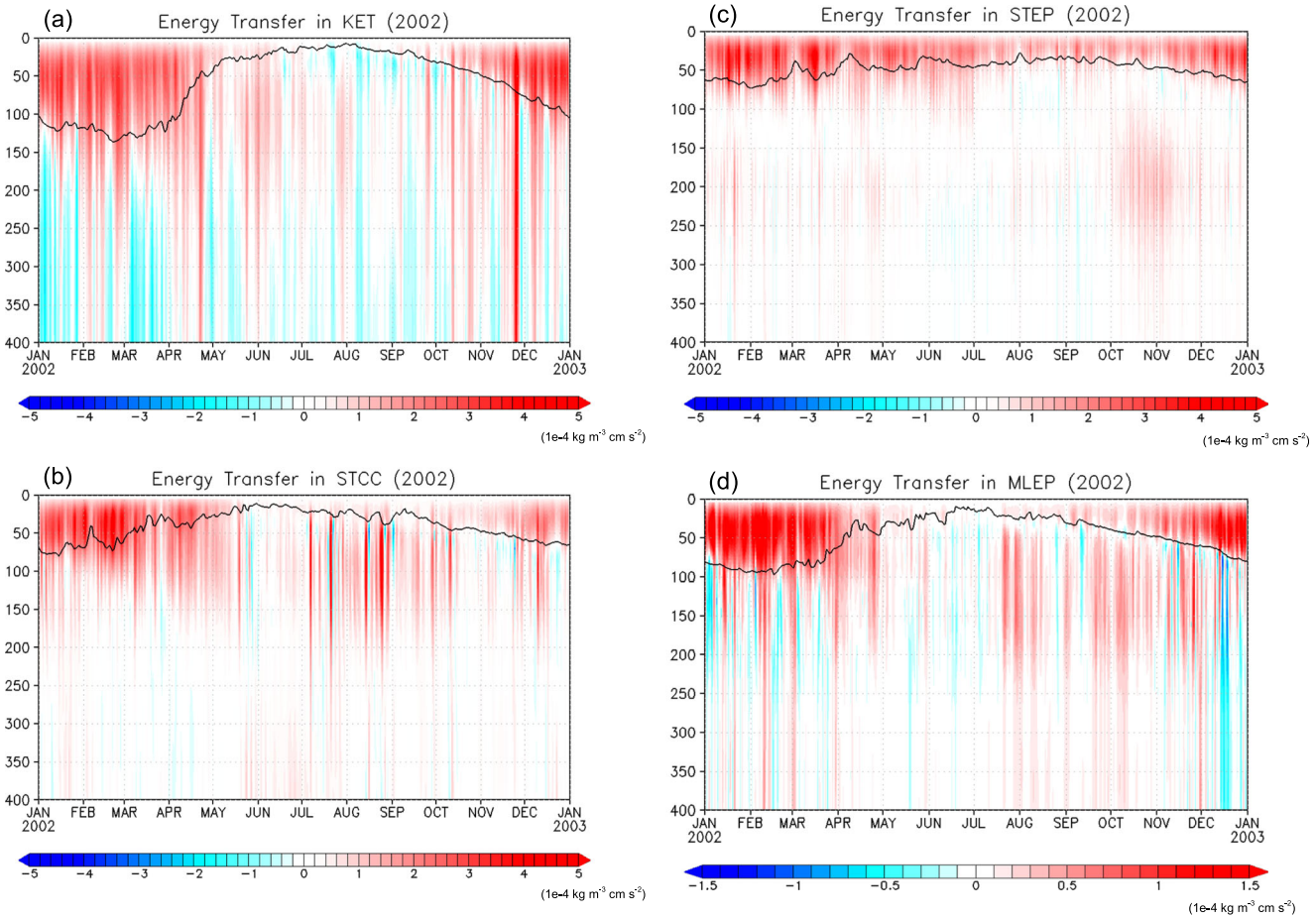

Fig. 8 Time variations of energy transformation from potential energy to kinetic energy ($<w'b'>_{xy}$) as a function of depth in 2002 in the 1/30° simulation. **a** KET, **b** STCC, **c** STEP, **d** MLEP, **e** SAWP, and **f** SAEP boxes. The color scale of **d**–**f** (from −1.5 to 1.5 (1e-4 kg m^{-3} cm s^{-1})) is different from that of **a**–**c** (from −5 to 5 (1e-4 kg m^{-3} cm s^{-1}))

to four times smaller than in high EKE regions (Fig. 11a–c). This suggests, in the MLEP region in winter, a competition between MLIs that produce submesoscales and instabilities at 100 km that produce mesoscale eddies.

On the other hand, MLIs in the subarctic regions (SAWP and SAEP), although still well resolved in the 1/30° simulation (Fig. 1), are no more the dominant process explaining submesoscales. Figures 9e, f and 10i, k emphasize that the wavelength of buoyancy flux and large vertical motions within the mixed layer in these regions is ~100 km in winter and summer. Time series of the RV and MLD rms values, and in particular their phase lags, also suggest that MLIs do not dominate the dynamics in winter (Fig. 6e, f). The RV rms values are still much larger in the 1/30° simulation than in the 1/10° simulation, with a nonnegligible seasonality, but there is no systematic phase lag with the RV and MLD time series (as it should occur when MLIs are the main mechanism producing submesoscales, see Q14, S14). Furthermore, there is no restratification in the 1/30° simulation, and on the contrary, the winter MLD is larger in this simulation compared to the 1/10° one (Fig. 6e, f). Since this restratification process is known to be mostly triggered by energetic frontal submesoscales, this means that submesoscales are either not energetic enough or do not have a strong frontal character (density fronts at small scale are not strong enough). This nonfrontal character is emphasized by the vertical section of the buoyancy fluxes (Fig. 8e, f) that are negative (downgradient) at the mixed-layer base during the fall. Spectral KE fluxes in the subarctic regions (Fig. 11e, f) further emphasize the impact of instabilities at 100 km: there is a net KE transfer to larger scales starting at 20 km, but this KE transfer is clearly intensified at 100 km.

These discrepancies, related to the MLI impact in winter, appear to agree with the velocity spectrum slope in the different regions (although interpretation of these slopes is not so meaningful as other diagnoses). Indeed, the velocity spectrum slope (not shown), in the high EKE regions is in k^{-2} in winter and k^{-3} in summer in the 1/30° simulation. The same spectrum slopes are observed in the MLEP region. But, in subarctic regions, these slopes are, respectively, in k^{-3} in winter and $k^{-3.5}$ in summer. A classical interpretation (Pierrehumbert et al. 1994; Held et al. 1995; Capet et al. 2008b; Klein and

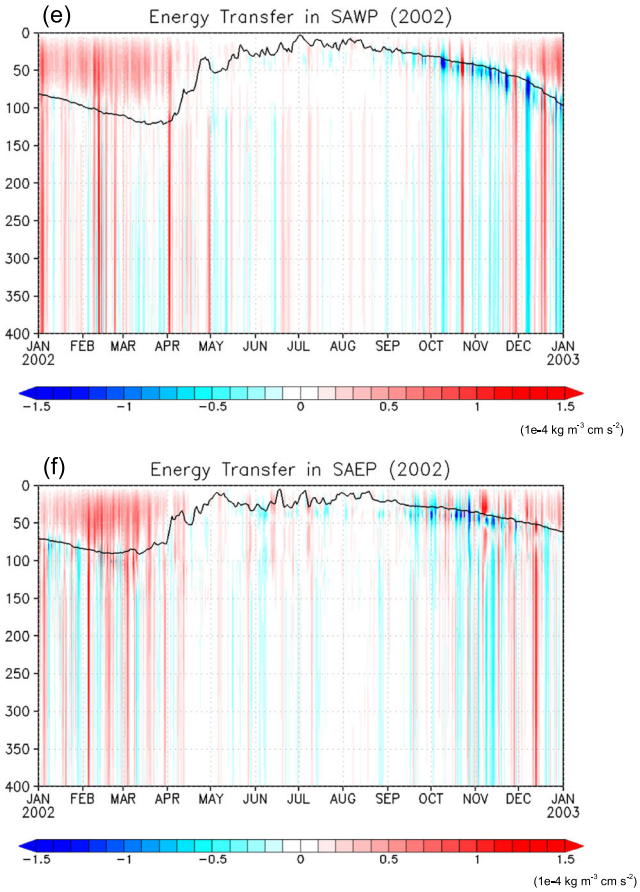

Fig. 8 (continued)

Lapeyre 2009) is that a k^{-2} slope for the velocity spectrum is a signature of the surface frontal character of the mesoscale and submesoscale turbulence, whereas a k^{-3} slope is more representative of the geostrophic turbulence. Thus, although all these diagnoses do not constitute a definite proof, they suggest that the winter production of submesoscales in subarctic regions may be partly explained by MLIs, but is certainly mostly explained by the direct enstrophy cascade, more energetic in winter because of the larger KE production at 100 km.

To further confirm the discrepancies between subarctic regions and the MLEP region, we again compare the KE time series in the 1/30° and 1/10° simulations. Figure 5g, h in the MLEP region clearly reveals that KE production at submesoscale leads to increase KE in the 10–100-km waveband. But there is no clear relationship between the KE time series in the 10–100-km range with those of larger scales. The KE transfer from 20 km to these larger scales (as emphasized by Fig. 11d) appears to be not large enough to affect significantly larger scales. These larger scales should be driven mostly by the KE production at 100 km (Fig. 9d). On the other hand, the KE magnitude in all of the time series (except for KE scales larger than 300 km) is much larger in the 1/30° simulation than in the 1/10° one (Fig. 5g, h), although the latter well resolves the 100-km scale. One classical explanation, usually invoked in geostrophic turbulence studies (Lapeyre et al. 1999; Joseph and Legras 2002; Lapeyre 2002), is that using a higher numerical resolution allows to better represent the velocity shear around mesoscale eddies (that acts as a dynamical barrier), which allows these eddies to be more coherent for a longer time instead of being quickly dissipated.

In terms of KE seasonality, the MLEP region displays a strong seasonal signal in the 1/30° simulation, not observed in the 1/10° simulation. But this is observed only for scales smaller than 200 km (black curve in Fig. 5g). Again, contribution of MLIs mostly explains this seasonality in this waveband with a peak in April (principally KE for scales smaller than 100 km: see purple curve in Fig. 5g). A similar seasonality is observed for scales smaller than 200 km in subarctic regions (black curves in Fig. 5i, k). But contribution of MLIs (through the KE for scales smaller than 100 km) is too small to explain this signal (purple curves in Fig. 5i, k). Furthermore, in the SAEP region, the KE peak (black curve in Fig. 5k) occurs in different months, either in April (in 2002) or in August (in 2003). The instability at 100 km is a strong candidate to explain this seasonality. But a better understanding of the dynamics in these subarctic regions requires first to better identify the mechanisms (and their potential seasonality) that force these instabilities at 100 km in the upper oceanic layers.

6 Discussion

This study focuses on the impact of scales between 16 and 50 km (we call submesoscales) on the dynamics in the North Pacific Ocean. This is done through the comparison of two numerical simulations, identical except for the numerical resolution (respectively, 1/30° and 1/10°, allowing to resolve physical wavelengths about 5 times the grid spacing). Thus, one simulation takes into account submesoscales, the other does not. Results indicate that submesoscale impact leads in all regions, not only to an increase of the KE by a factor up to 3, but also to a significant seasonality of this KE. These KE changes can be mostly explained by the MLIs within the upper oceanic layer in winter and the subsequent KE transfer to larger scale, which are, however, geographically dependent. In high KE regions, KE production is strongly intensified within the mixed layer in winter and mostly explained by MLIs that produce KE with large vertical motions at submesoscale within the upper oceanic layers, whereas the KE production is low with vertical motions at scales close to 100 km in summer. The resulting winter submesoscale KE is subsequently transferred to larger scales leading to a seasonal EKE evolution with a maximum in spring or summer. Thus, surface frontal dynamics at small scales appears to be the dominant mechanism explaining the strong KE increase and its seasonality. In regions with lower KE, in particular in subarctic regions, the

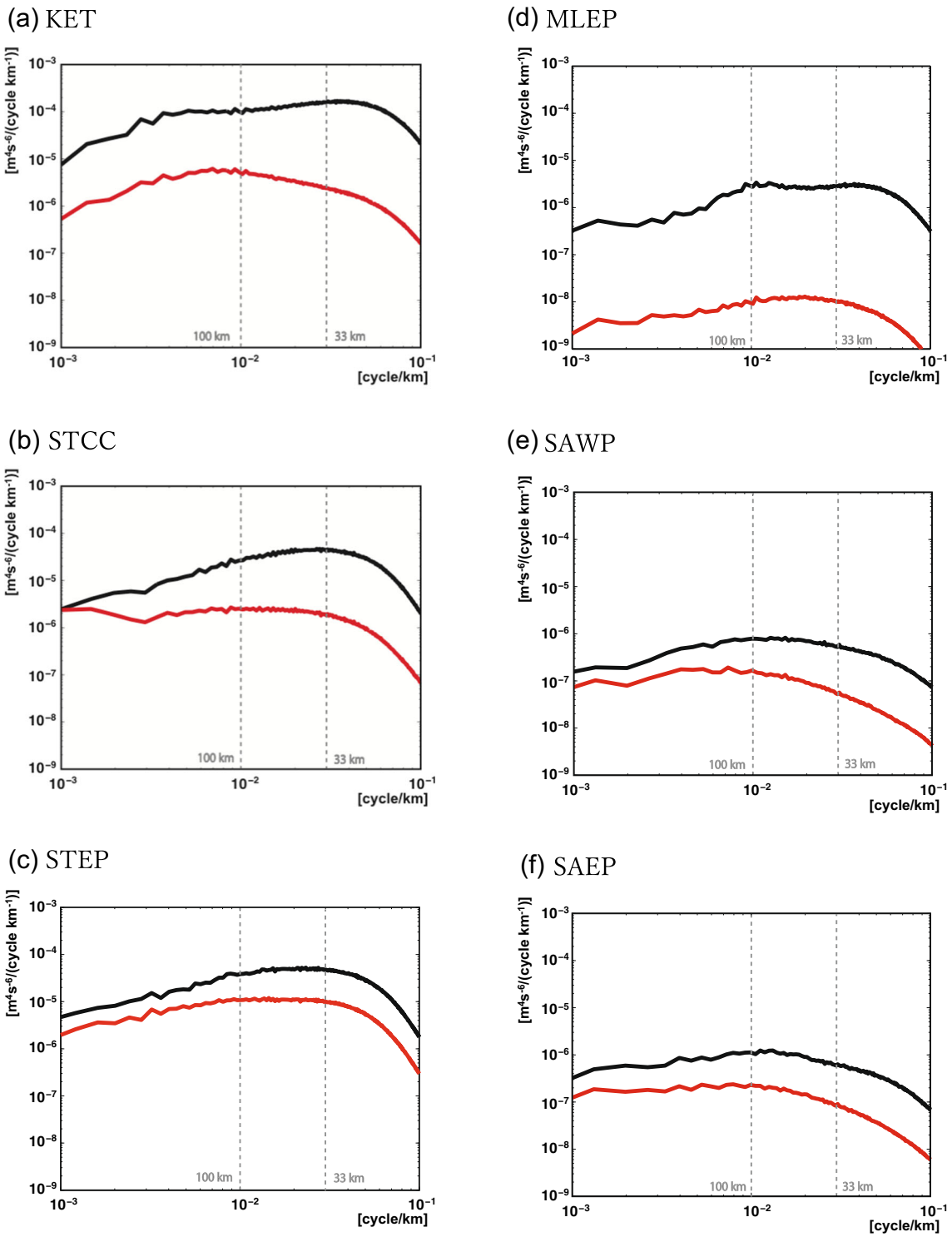

Fig. 9 Wavenumber spectra of buoyancy flux exhibiting energy transformation from potential energy to kinetic energy within the mixed layer (PK in Eq. (1)) in (*black curves*) winter (February and March) and (*red curves*) summer (from July to September) in the 1/30° simulation. **a** KET, **b** STCC, **c** STEP, **d** MLEP, **e** SAWP, and **f** SAEP boxes

surface frontal dynamics such as MLI is no more the main mechanism explaining the KE changes. Indeed, KE production is also intensified in winter but is mostly dominated year-round by instabilities at scales close to 100 km. Furthermore, the winter mixed layer is deepening instead of shallowing when submesoscales are taken into account. Since both simulations resolve well scales of the order of 100 km, it is suggested that the significant KE increase due to submesoscales in the lower

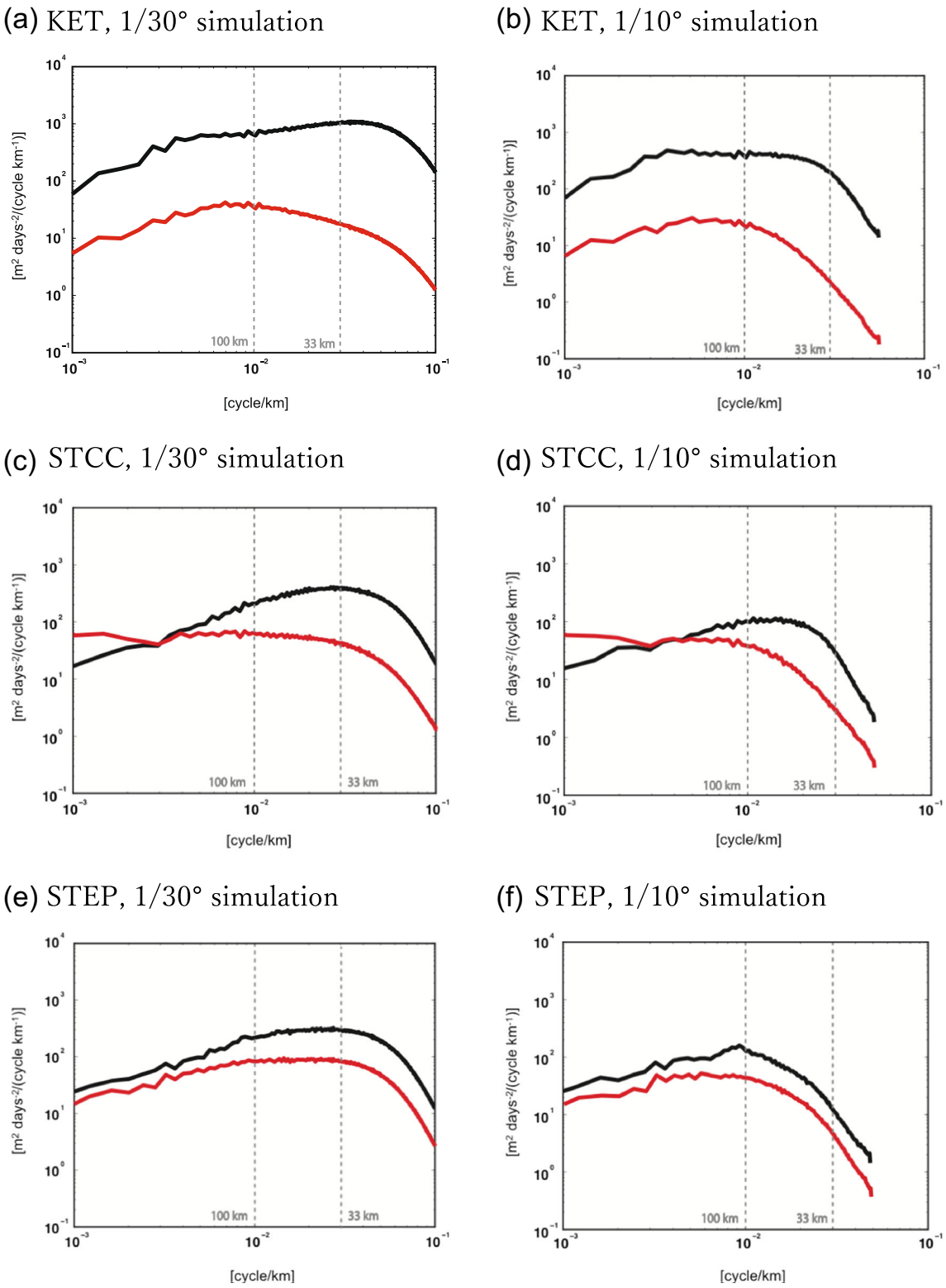

Fig. 10 Wavenumber spectra of vertical velocity within the mixed layer in (*black curves*) winter (February and March) and (*red curves*) summer (from July to September) in the **a**, **b** KET; **c**, **d** STCC; **e**, **f** STEP; **g**, **h** MLEP; **i**, **j** SAWP; and **k**, **l** SAEP boxes. (*Left*) 1/30° simulation and (*right*) 1/10° simulation

KE regions can be explained using arguments of geostrophic turbulence and, in particular, in terms of dynamical barriers (intensified at submesoscales) around mesoscale eddies that prevent these eddies to be dissipated too quickly.

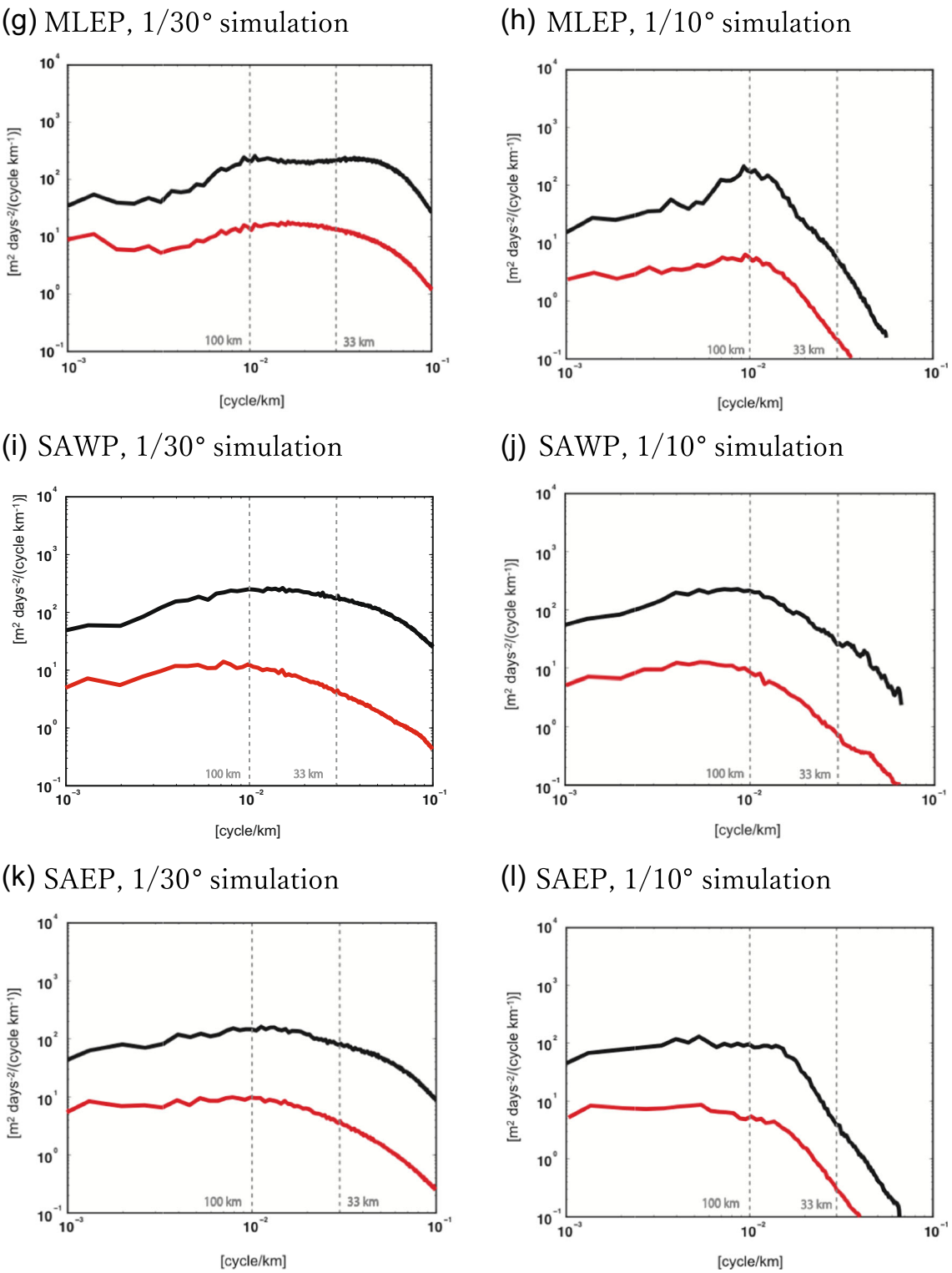

Fig. 10 (continued)

All these results need, however, to be checked more carefully, which is the focus of a future study. First, the type of instabilities that occur in the different regions at scales close to 100 km needs to be determined. The baroclinic instability of large-scale vertical current shears in the upper oceanic layers with a wavelength of the order of 100 km, corresponding to Charney-type instability, seems to be the most relevant one as reported in Qiu (1999) and Capet et al. (2016). This mechanism may be a candidate to explain the large-scale seasonality in lower EKE regions. But what causes these large-scale

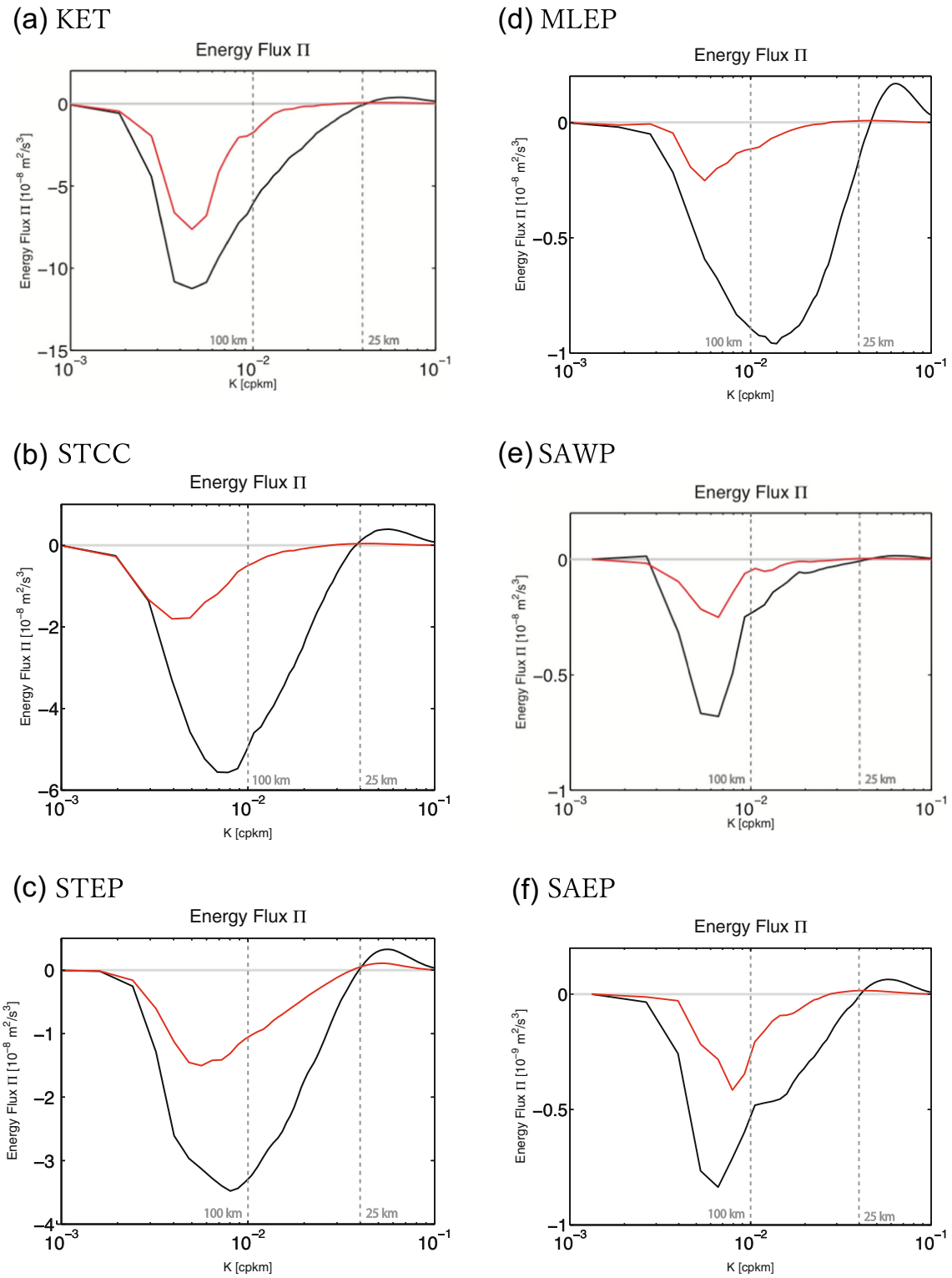

Fig. 11 Spectral KE fluxes using geostrophic velocities in winter (*black curves*) and summer (*red curves*) in the 1/30° simulation. **a** KET, **b** STCC, **c** STEP, **d** MLEP, **e** SAWP, and **f** SAEP boxes. Note that the vertical scales in each figure are different

instabilities in the different regions should be carefully investigated. Furthermore, the present results do not rule out that MLIs (although having scales well resolved in the 1/30° simulation) are more energetic in the lower KE regions than found in our study. Indeed, a higher resolution may lead to surface density fronts more intensified and, therefore, more likely to be affected by MLI. Production of submesoscales in the upper oceanic layers is also driven by other mechanisms such as

small-scale frontogenesis, wind induced frontal instabilities occurring at smaller scales. Thus, the surface frontal dynamics at small scales may be more energetic in these regions (see Thompson et al. 2016), but the geostrophic turbulent character is likely to still be the dominant one.

The relative impact of these different mechanisms, surface frontal dynamics at small scale and geostrophic turbulence driven by large-scale instabilities, needs also to be better quantified than is done in the present study. An energy budget that mixes the approaches followed by Roullet et al. (2012) and Chen et al. (2016) would be a suitable methodology. The simulations used in the present study are well appropriate to follow this methodology.

Acknowledgements The simulations were performed on the Earth Simulator under support of JAMSTEC. H.S. is supported by CANON Foundation. P.K. acknowledges the support of IFREMER (through the MOU IFREMER-JAMSTEC), CNRS (France), and the Agence Nationale pour la Recherche [Contract ANR-10-LABX-19-01 (LabexMER)]. B.Q. acknowledges Science Team support from NASA's SWOT mission NNX16AH66G. We appriciate comments from two reviewers, that significantly improved the manuscript.

References

Boccaletti G, Ferrari R, Fox-Kemper B (2007) Mixed layer instabilities and restratification. J Phys Oceanogr 37(9):2228–2250

Buckingham CE, Naveira Garabato AC, Thompson AF, Brannigan L, Lazar A, Marshall DP, George Nurser AJ, Damerell G, Heywood KJ, Belcher SE (2016) Seasonality of submesoscale flows in the ocean surface boundary layer. Geophys Res Lett 43(5):2118–2126

Callies J, Ferrari R, Klymak JM, Gula J (2015) Seasonality in submesoscale turbulence. Nat Commun 6:6862. doi:10.1038/ncomms7862

Callies J, Flierl G, Ferrari R, Fox-Kemper B (2016) The role of mixed-layer instabilities in submesoscale turbulence. J Fluid Mech 788:5–41

Capet X, Campos EJ, Paiva M (2008a) Submesoscale activity over the Argentinian shelf. Geophys Res Lett 35:2–6

Capet X, Klein P, Hua BL, Lapeyre G, Mcwilliams JC (2008b) Surface kinetic energy transfer in surface quasi-geostrophic flows. J Fluid Mech 604:165–174

Capet X, McWilliams JC, Molemaker MJ, Shchepetkin AF (2008c) Mesoscale to submesoscale transition in the California current system. Part III: energy balance and flux. J Phys Oceanogr 38(10):2256–2269

Capet X, Roullet G, Klein P, Maze G (2016) Intensification of upper-ocean submesoscale turbulence through Charney baroclinic instability. J Phys Oceanogr 46(11):3365–3384

Chen R, Flierl GR, Wunsch C (2014) A description of local and nonlocal eddy–mean flow interaction in a global eddy-permitting state estimate. J Phys Oceanogr 44(9):2336–2352

Chen R, Thompson AF, Flierl GR (2016) Time-dependent eddy-mean energy diagrams and their application to the ocean. J Phys Oceanogr 46(9):2827–2850

de Boyer Montégut C, Madec G, Fischer AS, Lazar A, Iudicone D (2004) Mixed layer depth over the global ocean: an examination of profile data and a profile-based climatology. J Geophys Res 109:C12003

Dufau C, Orsztynowicz M, Dibarboure G, Morrow R, Le Traon PY (2016) Mesoscale resolution capability of altimetry: present and future. J Geophys Res Oceans 121(7):4910–4927

Ferrari R, Wunsch C (2009) Ocean circulation kinetic energy: reservoirs, souces and sinks. Ann Rev Fluid Mech 41(1):253–282

Fox-Kemper B, Ferrari R, Hallberg R (2008) Parameterization of mixed layer eddies. Part I: theory and diagnosis. J Phys Oceanogr 38(6):1145–1165

Haines T, Marshall JC (1998) Gravitational, symmetric and baroclinic instability of the ocean mixed-layer. J Phys Oceanogr 28(4):634–658

Hakim GJ, Snyder C, Muraki DJ (2002) A new surface model for cyclone–anticyclone asymmetry. J Atmos Sci 59(16):2405–2420

Hanawa K, Talley LD (2001) Mode waters. In: Siedler G, Church J, Gould J (eds) Ocean circulation and climate: observing and modelling the global ocean. Academic, San Diego, pp 373–386

Hautala SL, Roemmich DH (1998) Subtropical mode water in the Northeast Pacific Basin. J Geophys Res Oceans 103(C6):13055–13066

Haza AC, Ozgökmen TM, Griffa A, Garaffo ZD, Piterbarg L (2012) Parameterization of particle transport at submesoscales in the Gulf Stream region using Lagrangian subgridscale models. Ocean Model 42:31–49

Held IM, Pierrehumbert RT, Garner ST, Swanson KL (1995) Surface quasigeostrophic dynamics. J Fluid Mechan 282:1–20

Joseph B, Legras B (2002) Relation between kinematic boundaries, stirring and barriers for the Antartic polar vortex. J Atmos Sci 59:1198–1212

Klein P, Lapeyre G (2009) The oceanic vertical pump induced by mesoscale and submesoscale turbulence. Annu Rev Mar Sci 1:351–375

Klein P, Hua BL, Lapeyre G, Capet X, Le Gentil S, Sasaki H (2008) Upper ocean turbulence from high-resolution 3D simulations. J Phys Oceanogr 38:1748–1763

Komori N, Takahashi K, Komine K, Motoi T, Zhang X, Sagawa G (2005) Description of sea-ice component of coupled ocean sea-ice model for the earth simulator (oifes). J Earth Simul 4:31–45

Lapeyre G (2002) Characterization of finite-time Lyapunov exponents and vectors in two-dimensional turbulence. Chaos 12:688–698

Lapeyre G, Klein P, Hua BL (1999) Does the tracer gradient vector align with the strain eigenvectors in 2-D turbulence? Phys Fluids 11:3729–3737

Lapeyre G, Klein P, Hua BL (2006) Oceanic restratification forced by surface frontogenesis. J Phys Oceanogr 36(8):1577–1590

Lévy M, Ferrari R, Franks PJS, Martin AP, Rivière P (2012a) Bringing physics to life at the submesoscale. Geophys Res Lett 39(14):L14602. doi:10.1029/2012GL052756

Lévy M, Resplandy L, Klein P, Capet X, Iovino D, Éthé C (2012b) Grid degradation of submesoscale resolving ocean models: benefits for offline passive tracer transport. Ocean Model 48:1–9

Masumoto Y et al (2004) A fifty-year eddy-resolving simulation of the world ocean: preliminary outcomes of OFES (OGCM for the Earth Simulator). J Earth Simul 1:35–56

McWilliams JC (2016) Submesoscale currents in the ocean. Proc R Soc A 472:20160117

McWilliams JC, Colas F, Molemaker MJ (2009) Cold filamentary intensification and oceanic surface convergence lines. Geophys Res Lett 36:1–5

Mensa JA, Garraffo Z, Griffa A, Özgökmen TM, Haza A, Veneziani M (2013) Seasonality of the submesoscale dynamics in the Gulf Stream region. Ocean Dyn 63:923–941

Nakamura N (1988) Scale selection of baroclinic instability—effects of stratification and nongeostrophy. J Atmos Sci 45(21):3253–3268

Noh Y, Kim HJ (1999) Simulations of temperature and turbulence structure of the oceanic boundary layer with the improved near-surface process. J Geophys Res Oceans 104(C7):15621–15634

Nonaka M, Sasai Y, Sasaki H, Taguchi B, Nakamura H (2016) How potentially predictable are midlatitude ocean currents? Sci Rep 6: 20153. doi:10.1038/srep20153

Onogi K et al (2007) The jra-25 reanalysis. J Met Soc Jap 85(3):369–432

Pacanowski RC, Griffies SM (1999) The MOM 3 manual, GFDL Ocean Group Tech. Rep. 4, 680 pp., NOAA/Geophys Fluid Dyn Lab, Princeton

Pierrehumbert RT, Held IM, Swanson KL (1994) Spectra of local and non-local two-dimensional turbulence. Chaos 4:1111–1116

Qiu B (1999) Seasonal eddy field modulation of the North Pacific Subtropical Countercurrent: TOPEX/POSEIDON observations and theory. J Phys Oceanogr 29(10):2471–2486

Qiu B, Scott R, Chen S (2008) Length scales of eddy generation and nonlinear evolution of the seasonally-modulated South Pacific Subtropical Countercurrent. J Phys Oceanogr 38(7):1515–1528

Qiu B, Chen S, Klein P, Sasaki H, Sasai Y (2014) Seasonal mesoscale and submesoscale eddy variability along the North Pacific Subtropical Countercurrent. J Phys Oceanogr 44(12):3079–3098

Roullet G, McWilliams JC, Capet X, Molemaker MJ (2012) Properties of steady geostrophic turbulence with isopycnal outcropping. J Phys Oceanogr 42(1):18–38

Sasaki H, Klein P (2012) SSH wavenumber spectra in the North Pacific from a high-resolution realistic simulation. J Phys Oceanogr 42(7): 1233–1241

Sasaki H, Klein P, Qiu B, Sasai Y (2014) Impact of oceanic scale-interactions on the seasonal modulation of ocean dynamics by the atmosphere. Nat Commun 5:5636. doi:10.1038/ncomms6636

Stone PH (1966) On non-geostrophic baroclinic instability. J Atmos Sci 23:3253–3268

Suga T, Motoki K, Aoki Y, Macdonald AM (2004) The North Pacific climatology of winter mixed layer and mode waters. J Phys Oceanogr 34(1):3–22

Thompson AF, Lazar A, Buckingham C, Naveira Garabato AC, Damerell GM, Heywood KJ (2016) Open-ocean submesoscale motions: a full seasonal cycle of mixed layer instabilities from gliders. J Phys Oceanogr 46(4):1285–1307

Tulloch R, Marshall J, Hill C (2011) Scales, growth rates and spectral fluxes of baroclinic instability in the ocean. J Phys Oceanogr 41(6): 1057–1076

Vallis GK (2006) Atmospheric and oceanic fluid dynamics. Cambridge University Press, 745 pp

Zhai X, Greatbatch RJ, Kohlmann JD (2008) On the seasonal variability of eddy kinetic energy in the Gulf Stream region. Geophys Res Lett 35(24):L24609. doi:10.1029/2008GL036412

Zhong Y, Bracco A (2013) Submesoscale impacts on horizontal and vertical transport in the Gulf of Mexico. J Geophys Res 118(10): 5651–5668